

SHAPE AS LINE SEGMENTS: ACCURATE AND FLEXIBLE IMPLICIT SURFACE REPRESENTATION

Anonymous authors

Paper under double-blind review

ABSTRACT

Distance field-based implicit representations like signed/unsigned distance fields have recently gained prominence in geometry modeling and analysis. However, these distance fields are reliant on the closest distance of points to the surface, introducing inaccuracies when interpolating along cube edges during surface extraction. Additionally, their gradients are ill-defined at certain locations, causing distortions in the extracted surfaces. To address this limitation, we propose Shape as Line Segments (SALS), an accurate and efficient implicit geometry representation based on attributed line segments, which can handle *arbitrary* structures. Unlike previous approaches, SALS leverages a differentiable *Line Segment Field* to implicitly capture the spatial relationship between line segments and the surface. Each line segment is associated with two key attributes, intersection flag and ratio, from which we propose edge-based dual contouring to extract a surface. We further implement SALS with a neural network, producing a new neural implicit presentation. Additionally, based on SALS, we design a novel learning-based pipeline for reconstructing surfaces from 3D point clouds. We conduct extensive experiments, showcasing the significant advantages of our methods over state-of-the-art methods. **We have included the source code in the *Supplemental Material*.**

1 INTRODUCTION

Various implicit geometry representations have emerged as powerful approaches in 3D vision, graphics, and robotics (Park et al., 2019; Takikawa et al., 2021; Wang et al., 2021; Mescheder et al., 2019; Chibane et al., 2020b). Unlike explicit representations that define surfaces through point clouds or polygon meshes, implicit representations describe surfaces as the isosurface of a scalar field. The signed/unsigned distance field (SDF/UDF) is among the most widely used implicit representations. Specifically, SDF captures the signed distance from a given point to the closest surface, where the sign is used to distinguish between the inside and outside. The surface can be extracted from SDFs easily via Marching Cubes (MC) (Lorenson & Cline, 1987), Dual Contouring (Ju et al., 2002) or their variants (Ju et al., 2002; Doi & Koide, 1991; Shen et al., 2021). However, SDF can only represent watertight shapes and cannot represent more general shapes, such as those with open boundaries and multi-layers, limiting its applications. By contrast, UDF, representing the absolute distance to the closest surface, allows for the representation of more general shapes. However, extracting surfaces from UDFs is much more difficult than SDFs, although several methods (Guillard et al., 2022; Ye et al., 2022; Chen et al., 2022; Zhang et al., 2023; Ren et al., 2023; Zhou et al., 2022) modified from MC and DC have been recently presented to extract surfaces from UDFs.

When extracting surfaces from SDFs and UDFs, MC-based methods compute the intersection point on each cube edge by interpolating the ratio of the distance values at the two endpoints of the edge. However, since this distance reflects the closest surface, inaccuracies may arise when there is another surface closer to one or both endpoints, leading to erroneous intersection points, as shown in Fig. 1a. Similarly, for DC-based methods (see Fig. 1b), an inaccurately calculated intersection point on the edge can lead to an incorrect solution of the quadratic error function within the cube. The differentiable properties of SDFs and UDFs, specifically their spatial gradients, are critical for surface extraction and offer notable advantages. However, the use of distance fields results in gradients that are meaningless in certain regions, such as at points equidistant from two surfaces (Fig. 1c), or even directly on the surface for UDFs. These limitations of SDFs and UDFs can introduce distortions during surface extraction.

Distance fields like SDF and UDF focus on the closest distances of individual spatial points to the surface. However, surface extraction from these fields often introduces distortions. As analyzed previously, both MC-based and DC-based methods rely on interpolation along each edge (line segment) of the cubes during surface extraction. Therefore, a natural approach is to shift the focus from individual points to line segments in 3D space. So can we build a field reflecting the spatial relationship between the line segment and the surface? Building on this intuition, we propose Shape as Line Segments (SALS), a precise and versatile implicit surface representation that centers on spatial line segments. SALS consists of two key components: **1)** a differentiable line segment field (LSF) that captures the spatial relationship between a query line segment and the surface, and **2)** an edge-based dual contouring approach to extract the surface from the LSF. As illustrated in Fig. 1d, our method focuses on line segments, avoiding the distortions typically introduced by SDFs and UDFs when extracting surfaces. Additionally, we establish a relationship between the unoriented surface normal and the proposed LSF, which facilitates surface extraction from LSFs. Based on SALS, we develop a neural surface representation technique and a surface reconstruction method from point clouds. Extensive experiments on diverse geometric data demonstrate the *significant* superiority of SALS over state-of-the-art methods.

In summary, we have made the following key contributions:

- a novel, accurate, and efficient implicit geometry representation, as well as its neural implementation, termed the line segment field (LSF), capable of handling shapes with arbitrary structures;
- a new surface extraction algorithm specifically designed for LSFs;
- a highly accurate, efficient, and generalizable learning pipeline for surface reconstruction from 3D point clouds.

2 RELATED WORK

Implicit Geometry Representation. Implicit geometry representations use the isosurface of a function or field to define a surface. Methods such as ONet (Mescheder et al., 2019), IF-Net (Chibane et al., 2020a), CONet (Peng et al., 2020), SPSR (Kazhdan & Hoppe, 2013), SAP (Peng et al., 2021), and POCO (Boulch & Marlet, 2022) employ the binary occupancy field (BOF) to represent surfaces by dividing the space into two regions—inside and outside the surface. This approach formulates the problem as binary classification, where the isosurface at a value of 0.5 defines the surface. Compared to BOFs, signed distance fields (SDFs) offer a more accurate representation by incorporating distance and using signs to indicate inside and outside regions. DeepSDF (Park et al., 2019) and DeepLS (Chabra et al., 2020) optimize latent vectors using an auto-decoder to refine SDFs, while NeuralPull (Baorui et al., 2021) and OSP (Ma et al., 2022) focus on the gradients of SDFs, pulling points onto the surface to guide SDFs. Some traditional methods can also be integrated with neural networks; for instance, DeepIMLS (Liu et al., 2021) and DOG (Wang et al., 2022) adapt implicit moving least-squares (IMLS) (Kolluri, 2008) to estimate SDFs. Recently, methods like (Wang et al., 2021; 2023; Meng et al., 2023) utilize SDFs in the volume rendering pipeline, and utilize image information as supervision to optimize the SDFs.

BOFs and SDFs are limited to representing watertight shapes and cannot handle more general geometries, such as open surfaces with boundaries or non-manifold surfaces. The unsigned distance field (UDF), the absolute value of SDF, is capable of representing more general shapes. NDF

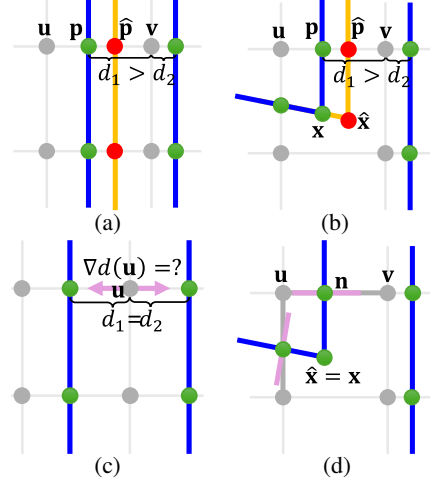


Figure 1: Visual comparisons of various implicit geometry representations and surface extraction methods. The gray points and gray line segments denote the vertices and edges of the cubes, respectively. The blue lines indicate the ground truth surface, while the orange lines represent the reconstructed surfaces. Green points mark the correctly interpolated points on the edges, whereas red points indicate interpolation errors. The pink arrows and pink lines represent oriented and unoriented normal vectors, respectively. (a) MC. (b) DC. (c) Gradient of distance fields. (d) Ours.

(Chibane et al., 2020b) employs 3D CNNs to regress UDFs from voxelized point clouds and generates dense point clouds by adjusting points according to UDF gradients. Building on previous work (Baorui et al., 2021; Ma et al., 2022), CAP-UDF (Zhou et al., 2022) applies a field consistency constraint to achieve consistency-aware UDFs. To improve reconstruction accuracy and generalizability, GeoUDF (Ren et al., 2023) leverages the geometric properties of point clouds to predict UDFs, decoupling UDF from its gradients. Methods like NuralUDF (Long et al., 2023) and NeUDF (Liu et al., 2023) incorporate UDFs to represent the objects in the volume rendering pipeline. Beyond distance fields, other types of implicit fields have also been developed to represent surfaces (Ye et al., 2022; Lu et al., 2024).

Surface Extraction from Implicit Geometry Representations. Marching Cubes (MC) (Lorenson & Cline, 1987) is the most widely used method for extracting surfaces from BOFs and SDFs. Marching Tetrahedra (Doi & Koide, 1991) and its variant (Shen et al., 2021) further divide the space into tetrahedra, a simpler cell than cubes. However, these methods are not applicable to UDFs due to the lack of inside/outside information. NDF (Chibane et al., 2020b) addresses this limitation by generating a much denser point cloud and then using the ball-pivoting algorithm (Bernardini et al., 1999) to create triangle meshes.

GIFS (Ye et al., 2022) employs a classifier to determine whether each edge of the cubes intersects the surface and then selects the closest match from the MC lookup table to extract triangles. In contrast, GeoUDF (Ren et al., 2023) uses UDF and its gradient to determine edge-surface intersections. MeshUDF (Guillard et al., 2022) and CAP-UDF (Zhou et al., 2022) adopt a different approach by using one vertex of the cube as a reference and computing the inner product of the UDF gradient with the remaining vertices. This converts a UDF into an SDF within the cube based on the sign of the inner product, allowing triangle extraction through MC. However, this method lacks robustness, often mispredicting faces at edges and corners. DCUDF (Hou et al., 2023) does not directly extract the surface, it first utilizes MC to extract an inflated surface, then the UDF gradients are used to refine the vertices.

Compared to these MC-based surface extraction techniques, dual contouring (DC) (Ju et al., 2002) preserves sharp surface features by solving a quadratic error function (QEF) in each cube. DC can be applied to BOFs, SDFs, and UDFs alike. Recently, NDC (Chen et al., 2022) improves DC by leveraging neural networks to solve QEFs, and DualMesh (Zhang et al., 2023) by introducing subsampling within each cube.

3 PROPOSED METHOD

As analyzed previously, existing implicit geometry representations, such as SDF and UDF, primarily focus on the closest distance from individual points to the surface, which can introduce distortion during surface extraction. Moreover, their differentiable properties, such as the gradient of UDF, become ill-defined at certain critical positions, further reducing the accuracy of the extracted surfaces.

Unlike previous approaches, our method is focused on spatial line segments to capture the geometric relationship between the segments and the surface. Specifically, we introduce a line segment field (LSF) to represent this spatial relationship (Sec. 3.1). We then propose edge-based dual contouring (E-DC) to extract the triangle mesh from the LSF (Sec. 3.2). Finally, based on LSF and E-DC, we propose neural shape representation (Sec. 3.3) and a new pipeline for reconstructing surfaces from 3D point clouds (Sec. 3.4).

3.1 DEFINITION OF LINE SEGMENT FIELD

Unlike existing implicit representations such as BOF and SDF, which concentrate on individual points in space, our line segment field (LSF) emphasizes spatial line segments. Let $\overline{uv} \in \Omega$ be a

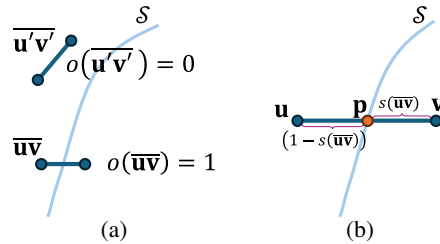


Figure 2: Visual illustration of the two attributes of the query segments: (a) o and (b) s .

query line segment with $\mathbf{u}, \mathbf{v} \in \mathbb{R}^3$ being the two end-points and Ω the set of all line segments in space and \mathcal{S} a 3D surface. The spatial relationship between $\overline{\mathbf{u}\mathbf{v}}$ and \mathcal{S} can be classified into two types: intersecting and non-intersecting. If intersecting, the intersection point lies on $\overline{\mathbf{u}\mathbf{v}}$, whose position can be represented as a linear combination of \mathbf{u} and \mathbf{v} .

Under such an intuition, we assign two attributes to the line segment $\overline{\mathbf{u}\mathbf{v}}$: a binary intersection flag $o(\overline{\mathbf{u}\mathbf{v}}) \in \{0, 1\}$ and an intersection ratio $s(\overline{\mathbf{u}\mathbf{v}}) \in [0, 1]$ ¹. More precisely, as illustrated in Fig. 2a, when $o(\overline{\mathbf{u}\mathbf{v}}) = 1$, it indicates the line segment $\overline{\mathbf{u}\mathbf{v}}$ intersects the surface \mathcal{S} , whereas $o(\overline{\mathbf{u}\mathbf{v}}) = 0$ signifies non-intersection. The intersection ratio $s(\overline{\mathbf{u}\mathbf{v}})$ specifies the location of the intersection point, denoted as $\mathbf{p} \in \mathbb{R}^3$, under the case $o(\overline{\mathbf{u}\mathbf{v}}) = 1$; moreover, we have $\mathbf{p} = s(\overline{\mathbf{u}\mathbf{v}})\mathbf{u} + (1 - s(\overline{\mathbf{u}\mathbf{v}}))\mathbf{v}$, as shown in Fig. 2b. Thus, by using the query line segments in Ω , the surface \mathcal{S} could be represented implicitly as

$$\mathcal{S} = \{s(\overline{\mathbf{u}\mathbf{v}})\mathbf{u} + (1 - s(\overline{\mathbf{u}\mathbf{v}}))\mathbf{v} \mid o(\overline{\mathbf{u}\mathbf{v}}) = 1, \overline{\mathbf{u}\mathbf{v}} \in \Omega\}. \quad (1)$$

Given that o and s characterize the local geometric properties of the surface \mathcal{S} around the query line segment $\overline{\mathbf{u}\mathbf{v}}$, we utilize the tangent plane of the surface at the intersection point \mathbf{p} to represent the local geometry. Specifically, let $\mathbf{n} \in \mathbb{R}^3$ be the unoriented normal vector at \mathbf{p} , and \mathbf{p}_0 any point on the tangent plane. It is worth noting that \mathbf{n} and \mathbf{p}_0 are fixed, independent of $\overline{\mathbf{u}\mathbf{v}}$. Theorem 1 demonstrates that the normal vector \mathbf{n} is parallel to the spatial gradient of s with respect to \mathbf{u} and \mathbf{v} , and provides a formal proof of this relationship.

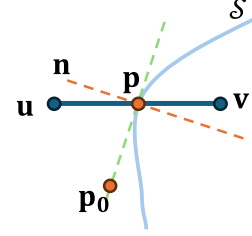


Figure 3: Local geometry of the surface near the intersection point.

Theorem 1. The unoriented normal vector \mathbf{n} at the intersection point \mathbf{p} between the line segment $\overline{\mathbf{u}\mathbf{v}}$ and surface \mathcal{S} is parallel to the spatial gradient of s , $\nabla_{\mathbf{u}}s$ and $\nabla_{\mathbf{v}}s$.

Proof. According to Fig. 3, the intersection ratio s is calculated as

$$s = \frac{\mathbf{n}^\top (\mathbf{v} - \mathbf{p}_0)}{\mathbf{n}^\top (\mathbf{v} - \mathbf{u})}.$$

Then, its gradient for \mathbf{u} and \mathbf{v} is

$$\nabla_{\mathbf{u}}s = \frac{\mathbf{n}^\top (\mathbf{v} - \mathbf{p}_0)}{(\mathbf{n}^\top (\mathbf{v} - \mathbf{u}))^2} \mathbf{n}, \quad \nabla_{\mathbf{v}}s = -\frac{\mathbf{n}^\top (\mathbf{v} - \mathbf{p}_0)}{(\mathbf{n}^\top (\mathbf{v} - \mathbf{u}))^2} \mathbf{n}.$$

Obviously, they are parallel to \mathbf{n} . □

3.2 SURFACE EXTRACTION FROM LSFs VIA EDGE-BASED DUAL CONTOURING

Building upon the principles of dual contouring (Ju et al., 2002), we propose edge-based dual contouring (E-DC) to extract the triangle meshes indicated by a given LSF. Specifically, as shown in Fig. 4a, for a given cube \mathcal{C} with its set of edges denoted as $\mathcal{E} = \{\overline{\mathbf{u}_i\mathbf{v}_i}\}_{i=1}^{12}$, the normal vector \mathbf{n}_i at $\overline{\mathbf{u}_i\mathbf{v}_i}$'s intersection point \mathbf{p}_i can be calculated through Theorem 1. Specifically, we use the gradient of the endpoint nearest to the intersection point to determine the normal vector's direction at that point,

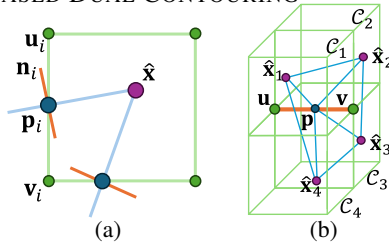


Figure 4: Visual illustration of surface extraction from an LSF. (a) QEF in each cube. (b) Triangle extraction in adjacency cubes.

$$\mathbf{n}_i = \begin{cases} \mathbf{n} = \nabla_{\mathbf{u}}s / \|\nabla_{\mathbf{u}}s\|, & \text{if } s(\overline{\mathbf{u}_i\mathbf{v}_i}) \leq 0.5 \\ \mathbf{n} = \nabla_{\mathbf{v}}s / \|\nabla_{\mathbf{v}}s\|, & \text{otherwise} \end{cases}. \quad (2)$$

The intersection point within the cube can be determined through optimizing the following quadratic error function (QEF):

$$\hat{\mathbf{x}} = \underset{\mathbf{x}}{\operatorname{argmin}} \sum_{\overline{\mathbf{u}_i\mathbf{v}_i} \in \mathcal{E}} (o_i(\mathbf{x} - \mathbf{p}_i)^\top \mathbf{n}_i)^2, \quad (3)$$

¹In practice, the inputs of o and s are the two endpoints of the line segments.

We refer readers to *Appendix B* for the solution to Eq. (3).

For any edge \overline{uv} that intersects the surface, i.e., $o(\overline{uv}) = 1$, it belongs to four cubes, denoted as $\{\mathcal{C}_i\}_{i=1}^4$, as shown in Fig. 4b. By solving the QEFs in these cubes, we obtain intersection points $\{\hat{\mathbf{x}}_i\}_{i=1}^4$ within these four cubes, which can be connected to form a quadrilateral. However, since quadrilateral meshes are not widely used in practice, it is necessary to subdivide the quadrilateral into triangles to generate a triangular mesh. Importantly, the intersection point \mathbf{p} on the edge \overline{uv} lies on the surface, enabling the quadrilateral to be divided into four triangles. By applying this process to all edges intersecting the surface, we can extract a triangle mesh from a given LSF.

Remark. Our proposed E-DC is significantly different from previous DC-based methods, such as NDC (Chen et al., 2022) and DualMesh (Zhang et al., 2023). Both NDC and DualMesh focus only on surface extraction from implicit representations, like SDFs or USDFs. NDC utilizes a trained network to predict the intersection point in each cube, and DualMesh adapts the traditional DC for neural UDFs. Differently, our proposed E-DC is an optimization-based surface extraction method, specifically designed to extract surfaces from LSF.

3.3 LSF-BASED NEURAL IMPLICIT REPRESENTATION

In this section, we employ a neural network to model the LSF of a given shape, where a lightweight MLP is trained with a set of ground-truth attributed line segments sampled in the space. After training, the MLP can predict the attributes o and s for any query line segment, producing the LSF, where we can utilize E-DC to extract a triangle mesh.

Technically, for a typical query line segment \overline{uv} , we concatenate its two endpoints \mathbf{u} and \mathbf{v} , which are then fed into an MLP parameterized with θ , outputting the corresponding values for o and s . It is worth noting that the concatenation is in an orderly manner, and the output intersection ratio s always indicates the ratio of the distance from the intersection point to the endpoint at the second concatenated position to the total length of the line segment, while the intersection flag o is independent of the concatenation order. Such a process is described as

$$\{o, s\} = \text{MLP}_{\theta}(\mathbf{u}||\mathbf{v}), \quad (4)$$

where $||$ denotes the concatenation of two vectors. The surface normal at the intersection points on the line segments can be determined by computing the gradient of s via backpropagation.

We optimize θ by minimizing the following loss function:

$$\mathcal{L} = \mathbb{E}_{\overline{uv} \in \Omega^*} (\lambda_1 \text{BCE}(o(\overline{uv}), o^*(\overline{uv})) + \lambda_2 o^*(\overline{uv}) |s(\overline{uv}) - s^*(\overline{uv})|), \quad (5)$$

where $\text{BCW}(\cdot, \cdot)$ represents Binary Cross Entropy, Ω^* is the set of sampled line segments, and o^* and s^* are the ground-truth intersection flag and ratio, respectively. See Sec. 4.1 for the experimental comparisons and analyses.

3.4 LEARNING LSFs FROM 3D POINT CLOUDS FOR SURFACE RECONSTRUCTION

Built upon the LSF introduced in Sec. 3.1, we propose a novel learning-based pipeline for reconstructing surfaces from 3D point clouds. After training, this pipeline is capable of predicting the LSF for any given 3D point cloud, enabling the subsequent application of our E-DC in Sec. 3.2 to extract a precise triangle mesh.

Denote by \mathbf{P} a 3D point cloud. Let $\mathcal{N}(\overline{uv}) = \{\mathbf{p}_i\}_{i=1}^K$ be a patch of K points associated with a typical query line segment \overline{uv} , which is derived by finding the K -nearest neighbors of the midpoint of \overline{uv} in \mathbf{P} . Also, let $\mathcal{N}_u(\overline{uv}) := \{\mathbf{p}_i - \mathbf{u}\}_{i=1}^K$ and $\mathcal{N}_v(\overline{uv}) := \{\mathbf{p}_i - \mathbf{v}\}_{i=1}^K$. Calculating the attributes of \overline{uv} against the underlying surface of \mathbf{P} is a local geometry problem, which pertains only to $\mathcal{N}(\overline{uv})$. Based on this

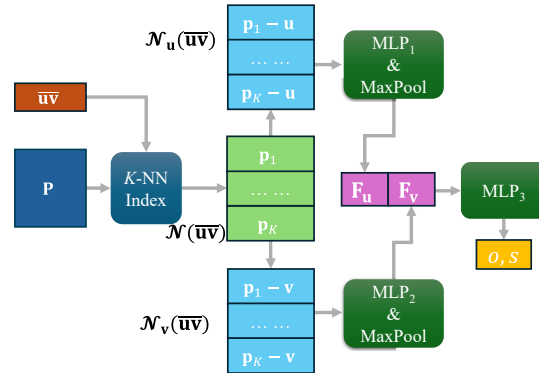


Figure 5: Flowchart of our learning-based surface reconstruction method from 3D point clouds.

observation, we construct our surface reconstruction pipeline using the following network architecture, as illustrated in Fig. 5: two MLPs followed by a MaxPool operation are first utilized to extract features from these two localized patches:

$$\mathbf{F}_u = \text{MaxPool}(\text{MLP}_{\theta_1}(\mathcal{N}_u(\overline{uv}))), \mathbf{F}_v = \text{MaxPool}(\text{MLP}_{\theta_2}(\mathcal{N}_v(\overline{uv}))), \quad (6)$$

where θ_1 and θ_2 are the sets of network parameters. The resulting features \mathbf{F}_u and \mathbf{F}_v are then concatenated and fed into another MLP parameterized with θ_3 to predict the corresponding o and s :

$$\{o, s\} = \text{MLP}_{\theta_3}(\mathbf{F}_u || \mathbf{F}_v). \quad (7)$$

We minimize the loss function defined in Eq. (5) to train the network. See Sec. 4.1 for the experimental comparisons and analyses.

4 EXPERIMENTS

4.1 EVALUATION ON NEURAL IMPLICIT REPRESENTATION

Datasets. We randomly selected 50 shapes from the ABC dataset (Koch et al., 2019) to conduct experiments. Additionally, we constructed a more complex dataset named *non-manifold ABC* dataset, in which each of the 50 shapes was produced by intersecting two randomly selected shapes for creating non-manifold structures. Besides, we utilized shapes from other commonly used datasets, including open-boundary clothes from the DeepFashion3D dataset (Zhu et al., 2020), and complex shapes from the Famous dataset (Erler et al., 2020). All shapes were rescaled to a bounding cube with an edge length of 2 and centered at the origin.

Implementation Details. We employed an 8-layer MLP, with each layer comprising 512 neurons. All layers, except the final one, use the *Softplus* activation function ($\beta = 100$, as recommended in (Atzmon & Lipman, 2020)). The final layer consists of 2 neurons, followed by a *Sigmoid* activation function. We sampled 10 million line segments within the space to optimize the MLP. The model was trained for 100,000 epochs with a batch size of 10,000, using the ADAMW optimizer (Loshchilov, 2017) with an initial learning rate of 0.001. The learning rate was progressively adjusted using cosine annealing (Loshchilov & Hutter, 2016), with a minimum learning rate of 10^{-5} . When extracting the surface, the resolution of grids used in E-DC was set to 128, **keeping the same as the baseline methods**. To measure the reconstructed quality quantitatively, we sample 10^5 points from each surface to calculate L1-CD, Normal Consistency (NC), and F-Score with the threshold of 0.005 and 0.01 with respect to the ground truth surfaces.

Methods under Comparison. We compared our method against three commonly used implicit geometry representations, i.e., BOF, SDF, and UDF, using MLPs with the same architectures as ours for modeling. For surface extraction methods from implicit representations, we benchmarked SALS against MC (Lorensen & Cline, 1987), NDC (Chen et al., 2022), MeshUDF (Guillard et al., 2022), DCUDF (Hou et al., 2023), and DualMesh (Zhang et al., 2023). Additionally, we included two recently proposed methods, i.e., NGLOD (Takikawa et al., 2021) and UODF (Lu et al., 2024), maintaining the settings consistent with their original papers.

Results. We quantitatively compared those methods on the ABC and non-manifold ABC datasets in Table 1, where it can be seen that our method outperforms the other methods in terms of all metrics, especially on the non-manifold ABC dataset. The visual results are shown in Fig. 6, and obviously, the surfaces represented by our method can preserve detailed structures, including the non-manifold ones. Our method only built upon a simple MLP can represent shapes with higher accuracy, compared with the relatively complex methods, such as NGLOD and UODF, which is credited to our novel LSF. BOF represents the probability that a query point is either inside or outside the surface, and it is less accurate than other methods. Surfaces extracted from the distance fields present distortion at the detailed regions since they rely on the closest distance of individual points to the surface. Therefore, under the same MLP settings, these methods exhibit low representation accuracy. UODF utilizes SPSR (Kazhdan & Hoppe, 2013) to extract the surface, decreasing its accuracy. When handling shapes with non-manifold structures, the representation accuracy of both BOF and SDF drops significantly, as they are inherently unable to represent non-manifold geometry. While UDF can represent non-manifold structures, its reliance on gradients for surface extraction leads to inaccuracies, particularly at non-manifold regions, which in turn reduces representation

Table 1: Quantitative comparisons of different neural implicit representations with various surface extraction methods on the ABC and non-manifold ABC datasets. The best results are highlighted in **bold**.

	Methods	# Param	CD (10^{-3}) ↓	NC ↑	F1-0.005 ↑	F1-0.01 ↑
ABC	Neural BOF + MC (Lorensen & Cline, 1987)	1.84M	6.385	0.911	0.528	0.941
	Neural SDF + MC (Lorensen & Cline, 1987)	1.84M	5.810	0.966	0.618	0.946
	Neural SDF + NDC (Chen et al., 2022)	2.07M	4.607	0.967	0.627	0.963
	NGLOD (Takikawa et al., 2021)	10.14M	6.070	0.957	0.541	0.919
	Neural UDF + MeshUDF (Guillard et al., 2022)	1.84M	5.075	0.967	0.578	0.937
	Neural UDF + NDC (Chen et al., 2022)	2.07M	4.944	0.955	0.584	0.942
	Neural UDF + DCUDF (Hou et al., 2023)	1.84M	4.593	0.971	0.625	0.962
	Neural UDF + DualMesh (Zhang et al., 2023)	1.84M	4.725	0.978	0.609	0.952
	UODF (Lu et al., 2024)	5.55M	4.794	0.977	0.603	0.953
	SALS (Ours)	1.84M	4.493	0.980	0.638	0.965
Non-manifold ABC	Neural BOF + MC (Lorensen & Cline, 1987)	1.84M	14.371	0.886	0.356	0.810
	Neural SDF + MC (Lorensen & Cline, 1987)	1.84M	13.567	0.929	0.422	0.822
	Neural SDF + NDC (Chen et al., 2022)	2.07M	8.642	0.944	0.422	0.835
	NGLOD (Takikawa et al., 2021)	10.14M	10.250	0.913	0.301	0.750
	Neural UDF + MeshUDF (Guillard et al., 2022)	1.84M	6.465	0.948	0.392	0.855
	Neural UDF + NDC (Chen et al., 2022)	2.07M	14.893	0.932	0.382	0.849
	Neural UDF + DCUDF (Hou et al., 2023)	1.84M	6.111	0.954	0.427	0.886
	Neural UDF + DualMesh (Zhang et al., 2023)	1.84M	6.706	0.961	0.367	0.823
	UODF (Lu et al., 2024)	5.55M	6.746	0.953	0.367	0.835
	SALS (Ours)	1.84M	5.949	0.963	0.437	0.889

accuracy. Additionally, Fig. 7 visualizes the results of our method on other general shapes from the DeepFashion3D and Famous datasets. Obviously, the extracted surface can preserve detailed structures. We refer the readers to Appendix C for more results.

4.2 EVALUATION ON SURFACE RECONSTRUCTION FROM 3D POINT CLOUDS

Datasets. We employed a *significantly smaller* training set compared to previous methods, comprising 100 shapes selected from the Thingi10K dataset (Zhou & Jacobson, 2016) to train our network. For testing, we utilized the ABC and non-manifold ABC datasets, as well as more diverse shapes from the DeepFashion3D (Zhu et al., 2020), Synthetic Rooms (Peng et al., 2020) and Waymo (Sun et al., 2020) datasets. Each shape contains 40,000 randomly sampled points.

Implementation Details. Each of the three MLPs in Fig. 5 consists of 4 layers, with 256 neurons per layer. All layers, except the final one, used the *LeakyReLU* activation function. The patch size for K -NN is set to $K = 20$. The network was trained for 400 epochs with a batch size of 4, where 5120 line segments were sampled for each shape at each iteration. The optimizer used was ADAMW (Loshchilov, 2017), with an initial learning rate of 0.001, which was adjusted via cosine annealing (Loshchilov & Hutter, 2016) to a minimum learning rate of 10^{-5} . The grid resolution was set to 128 when performing surface extraction, **keeping the same as the baseline methods**.

Methods under Comparison. We compared our method against SOTA surface reconstruction methods, including POCO (Boulch & Marlet, 2022), GIFS (Ye et al., 2022), CAP-UDF (Zhou et al., 2022), and GeoUDF (Ren et al., 2023), whose settings were maintained the same as their original papers for fair comparisons.

Results. Table 2 lists the quantitative results of different methods. It is obvious that our method outperform baseline methods, especially on the non-manifold ABC datasets. Achieving such high-

Table 2: Quantitative comparisons of 3D point cloud-based surface reconstruction methods on the ABC and non-manifold ABC datasets. The best results are highlighted in **bold**.

	Method	# Param	CD (10^{-3}) ↓	NC ↑	F1-0.005 ↑	F1-0.01 ↑
ABC	POCO (Boulch & Marlet, 2022)	12.79M	8.855	0.952	0.558	0.886
	GIFS (Ye et al., 2022)	3.68M	5.726	0.940	0.471	0.923
	CAP-UDF (Zhou et al., 2022)	0.46M	5.308	0.958	0.554	0.924
	GeoUDF (Ren et al., 2023)	0.77M	4.678	0.970	0.615	0.957
	SALS (Ours)	1.07M	4.560	0.973	0.630	0.962
Non-manifold ABC	POCO (Boulch & Marlet, 2022)	12.79M	16.830	0.905	0.269	0.658
	GIFS (Ye et al., 2022)	3.68M	7.078	0.927	0.305	0.826
	CAP-UDF (Zhou et al., 2022)	0.46M	7.280	0.929	0.357	0.833
	GeoUDF (Ren et al., 2023)	0.77M	6.230	0.950	0.410	0.869
	SALS (Ours)	1.07M	6.033	0.951	0.425	0.883

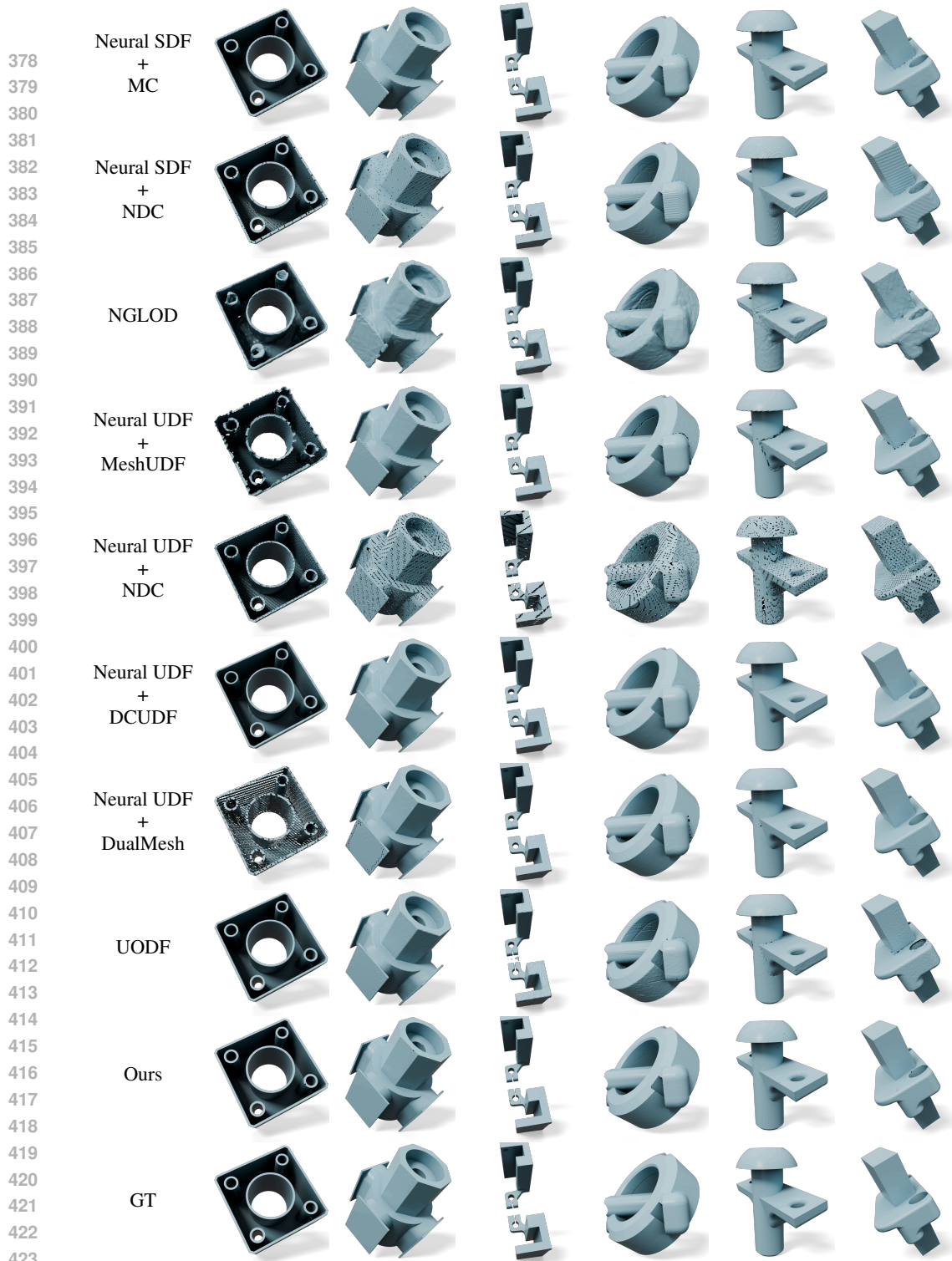
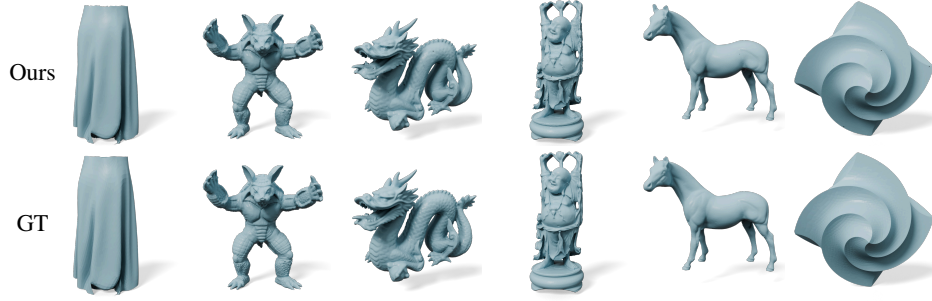
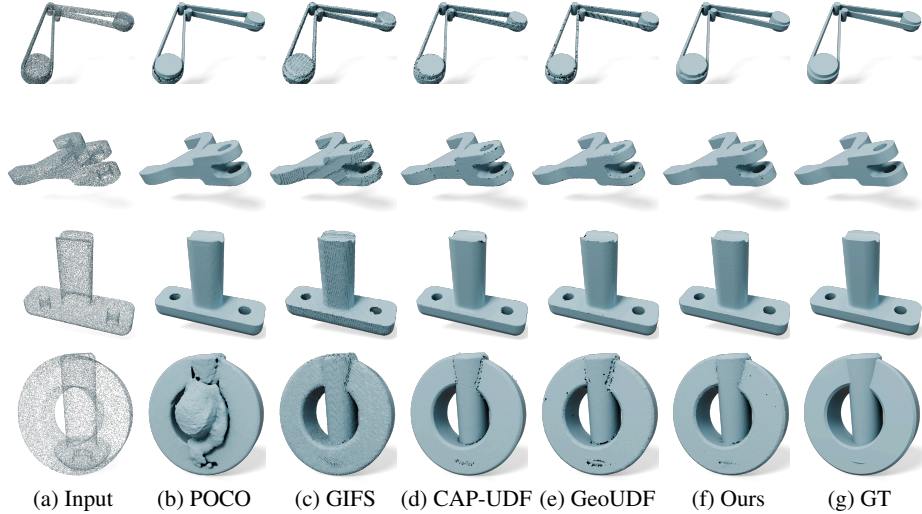


Figure 6: Visual comparisons of different neural implicit representations. [Q Zoom in to see details.](#) precision reconstruction with so little training data and such a simple network structure is primarily attributed to our proposed implicit geometry representation and the effective local geometry modeling. The visual comparison is shown in Fig. 8, where our method can preserve detailed structures. Furthermore, Figs. 9 and 10 present the results of our method applied to additional shapes and scenes from the DeepFashion3D, Synthetic Rooms, and Waymo datasets. Notably, the reconstructed surfaces successfully capture fine structural details, highlighting the strong generalizability and robustness of our approach across diverse datasets. We refer the reader to Appendix D for more results.

Figure 7: Visual results on the DeepFashion3D and Famous datasets. **Q** Zoom in to see details.Figure 8: Visual comparisons of different point cloud surface reconstruction methods. **Q** Zoom in to see details.

4.3 ABLATION STUDY

We conducted comprehensive ablation studies on the ABC dataset to show the rationality of our design.

Spatial gradient of s . Theorem 1 demonstrates that the normal vector at the intersection point is parallel to the spatial gradient of s , which is crucial for accurate surface extraction. To validate this, we conducted experiments where, instead of directly utilizing the normal vectors at the intersection points, we employed the center of the intersection points within each cube as the solution for the QEF during surface extraction from the LSF. As shown in Fig 11, removing normals from E-DC significantly reduces the ability to capture fine surface details, as normals are essential for describing detailed structures. On the other way, this also confirms the validity of Theorem 1.

E-DC Resolution. We evaluated the accuracy of the extracted surfaces under varying resolutions of E-DC, with the numerical results presented in

Table 3: Representation accuracy under various resolutions of E-DC.

Res.	Inf. Time	GPU Mem.	CD (10^{-3})	NC	F1-0.005 \uparrow	F1-0.01 \uparrow
64	1.099s	1.55GB	4.731	0.963	0.606	0.952
128	6.682s	4.78GB	4.493	0.980	0.638	0.965
192	19.663s	11.99GB	4.490	0.981	0.638	0.965

Table 3. At lower resolutions, such as 64, the representation accuracy decreases significantly. However, increasing the resolution beyond 128, for instance to 192, does not yield substantial improvements in accuracy despite requiring more computational resources. We also refer reviewers to Fig. 15 of Appendix C for the visual results.

K -NN Size of Query Line Segments. When computing the LSF for query line segments from a point cloud, the size of the K -NN patch is a critical hyperparameter. To evaluate its impact, we tested the accuracy of our method under different values of K .

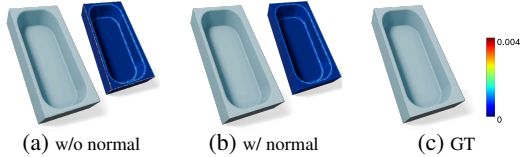


Figure 11: Extracted surfaces using E-DC without and with normal.

Table 4: Point cloud surface reconstruction accuracy under different K -NN sizes.

K	CD (10^{-3})	NC	F1-0.005 \uparrow	F1-0.01 \uparrow
10	6.367	0.903	0.489	0.848
20	4.560	0.973	0.630	0.962
50	14.370	0.657	0.164	0.415

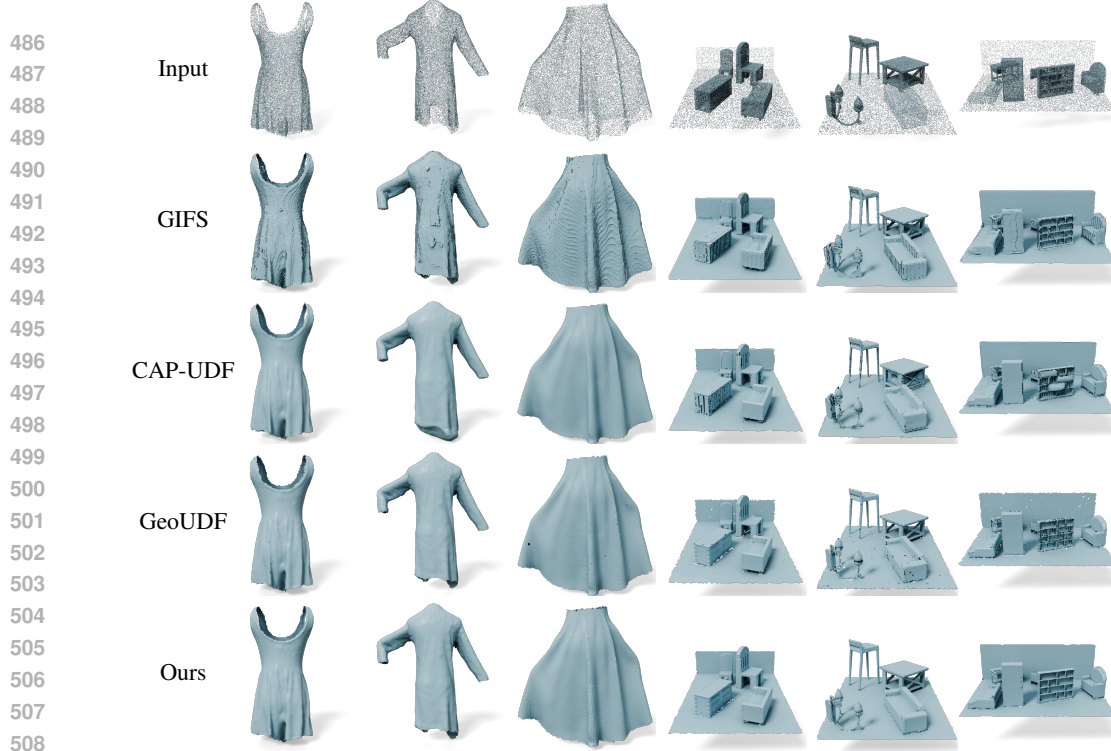


Figure 9: Visual results of point cloud surface reconstruction methods on DeepFashion3D and Synthetic Rooms datasets. [Zoom in to see details.](#)

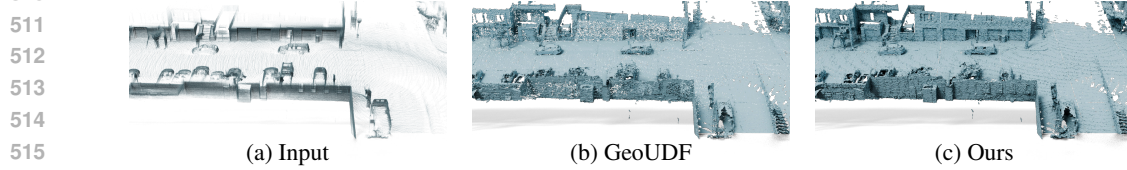


Figure 10: Visual results of point cloud surface reconstruction methods on the Waymo dataset. [Zoom in to see details.](#)

As listed in Table 4, setting K either too large or too small leads to a noticeable decrease in reconstruction accuracy. We also refer reviewers to Fig. 20 of Appendix C for visual results.

Point Cloud Density. We evaluated the reconstruction accuracy of our method across different point cloud densities to verify its robustness. The numerical results, presented in Table 5, indicate a slight decrease in accuracy when the point clouds become sparser. However, increasing the number of points does not result in significant improvements in accuracy, suggesting its robustness. We also refer reviewers to Fig. 19 in Appendix for visual results.

Table 5: Point cloud surface reconstruction accuracy under different numbers of input points.

# Points	CD (10^{-3})	NC	F1-0.005 \uparrow	F1-0.01 \uparrow
1×10^4	4.842	0.953	0.608	0.948
4×10^4	4.560	0.973	0.630	0.962
10×10^4	4.514	0.977	0.636	0.964

5 CONCLUSION

We have introduced SALS, an accurate and flexible implicit geometry representation. We began by analyzing the primary limitations of existing implicit representations, which are predominantly based on distance fields. In contrast, SALS focuses on the spatial relationship between line segments and the surface, resulting in greater accuracy than prior methods. Leveraging SALS, we proposed both a neural shape representation approach and a learning pipeline of surface reconstruction from point clouds, achieving superior performance over state-of-the-art methods. The effectiveness and advantages of SALS underscore its potential to significantly advance the field of 3D geometric modeling and processing.

ETHICS STATEMENT

SALS is an accurate and versatile implicit surface representation capable of representing arbitrary shapes. We have read and adhere to the Code of Ethics of ICLR 2025. To the best of our knowledge, this study does not involve ethics issues.

REPRODUCIBILITY STATEMENT

We have included the source code in the Supplementary Material submitted to the system, and detailed instructions for its usage are outlined in the ‘README.md’ file.

REFERENCES

- Matan Atzmon and Yaron Lipman. Sald: Sign agnostic learning with derivatives. *arXiv preprint arXiv:2006.05400*, 2020.
- Ma Baorui, Han Zhizhong, Liu Yu-Shen, and Zwicker Matthias. Neural-pull: Learning signed distance functions from point clouds by learning to pull space onto surfaces. In *International Conference on Machine Learning*, volume 139, pp. 7246–7257, 2021.
- Fausto Bernardini, Joshua Mittleman, Holly Rushmeier, Cláudio Silva, and Gabriel Taubin. The ball-pivoting algorithm for surface reconstruction. *IEEE transactions on visualization and computer graphics*, 5(4):349–359, 1999.
- Alexandre Boulch and Renaud Marlet. Poco: Point convolution for surface reconstruction. In *Proceedings of the IEEE/CVF Conference on Computer Vision and Pattern Recognition*, pp. 6302–6314, June 2022.
- Rohan Chabra, Jan E Lenssen, Eddy Ilg, Tanner Schmidt, Julian Straub, Steven Lovegrove, and Richard Newcombe. Deep local shapes: Learning local sdf priors for detailed 3d reconstruction. In *European Conference on Computer Vision*, pp. 608–625. Springer, 2020.
- Zhiqin Chen, Andrea Tagliasacchi, Thomas Funkhouser, and Hao Zhang. Neural dual contouring. *ACM Transactions on Graphics (TOG)*, 41(4):1–13, 2022.
- Julian Chibane, Thiemo Alldieck, and Gerard Pons-Moll. Implicit functions in feature space for 3d shape reconstruction and completion. In *Proceedings of the IEEE/CVF Conference on Computer Vision and Pattern Recognition*, pp. 6970–6981, June 2020a.
- Julian Chibane, Gerard Pons-Moll, et al. Neural unsigned distance fields for implicit function learning. *Advances in Neural Information Processing Systems*, 33:21638–21652, 2020b.
- Akio Doi and Akio Koide. An efficient method of triangulating equi-valued surfaces by using tetrahedral cells. *IEICE TRANSACTIONS on Information and Systems*, 74(1):214–224, 1991.
- Philipp Erler, Paul Guerrero, Stefan Ohrhallinger, Niloy J Mitra, and Michael Wimmer. Points2surf learning implicit surfaces from point clouds. In *European Conference on Computer Vision*, pp. 108–124. Springer, 2020.
- Benoit Guillard, Federico Stella, and Pascal Fua. Meshudf: Fast and differentiable meshing of unsigned distance field networks. In *European Conference on Computer Vision*, pp. 576–592, 2022.
- Fei Hou, Xuhui Chen, Wencheng Wang, Hong Qin, and Ying He. Robust zero level-set extraction from unsigned distance fields based on double covering. *ACM Transactions on Graphics (TOG)*, 42(6):1–15, 2023.
- Tao Ju, Frank Losasso, Scott Schaefer, and Joe Warren. Dual contouring of hermite data. In *Proceedings of the 29th annual conference on Computer graphics and interactive techniques*, pp. 339–346, 2002.

- Michael Kazhdan and Hugues Hoppe. Screened poisson surface reconstruction. *ACM Transactions on Graphics*, 32(3):1–13, 2013.
- Sebastian Koch, Albert Matveev, Zhongshi Jiang, Francis Williams, Alexey Artemov, Evgeny Burnaev, Marc Alexa, Denis Zorin, and Daniele Panozzo. Abc: A big cad model dataset for geometric deep learning. In *Proceedings of the IEEE/CVF conference on computer vision and pattern recognition*, pp. 9601–9611, 2019.
- Ravikrishna Kolluri. Provably good moving least squares. *ACM Transactions on Algorithms*, 4(2): 1–25, 2008.
- Shi-Lin Liu, Hao-Xiang Guo, Hao Pan, Peng-Shuai Wang, Xin Tong, and Yang Liu. Deep implicit moving least-squares functions for 3d reconstruction. In *Proceedings of the IEEE/CVF Conference on Computer Vision and Pattern Recognition*, pp. 1788–1797, June 2021.
- Yu-Tao Liu, Li Wang, Jie Yang, Weikai Chen, Xiaoxu Meng, Bo Yang, and Lin Gao. Neudf: Leaning neural unsigned distance fields with volume rendering. In *Proceedings of the IEEE/CVF Conference on Computer Vision and Pattern Recognition*, pp. 237–247, 2023.
- Xiaoxiao Long, Cheng Lin, Lingjie Liu, Yuan Liu, Peng Wang, Christian Theobalt, Taku Komura, and Wenping Wang. Neuraludf: Learning unsigned distance fields for multi-view reconstruction of surfaces with arbitrary topologies. In *Proceedings of the IEEE/CVF Conference on Computer Vision and Pattern Recognition*, pp. 20834–20843, 2023.
- William E Lorensen and Harvey E Cline. Marching cubes: A high resolution 3d surface construction algorithm. *ACM siggraph computer graphics*, 21(4):163–169, 1987.
- I Loshchilov. Decoupled weight decay regularization. *arXiv preprint arXiv:1711.05101*, 2017.
- Ilya Loshchilov and Frank Hutter. Sgdr: Stochastic gradient descent with warm restarts. *arXiv preprint arXiv:1608.03983*, 2016.
- Yujie Lu, Long Wan, Nanyang Ding, Yulong Wang, Shuhan Shen, Shen Cai, and Lin Gao. Unsigned orthogonal distance fields: An accurate neural implicit representation for diverse 3d shapes. In *Proceedings of the IEEE/CVF Conference on Computer Vision and Pattern Recognition*, pp. 20551–20560, 2024.
- Baorui Ma, Yu-Shen Liu, and Zhizhong Han. Reconstructing surfaces for sparse point clouds with on-surface priors. In *Proceedings of the IEEE/CVF Conference on Computer Vision and Pattern Recognition*, pp. 6315–6325, June 2022.
- Xiaoxu Meng, Weikai Chen, and Bo Yang. Neat: Learning neural implicit surfaces with arbitrary topologies from multi-view images. In *Proceedings of the IEEE/CVF Conference on Computer Vision and Pattern Recognition*, pp. 248–258, 2023.
- Lars Mescheder, Michael Oechsle, Michael Niemeyer, Sebastian Nowozin, and Andreas Geiger. Occupancy networks: Learning 3d reconstruction in function space. In *Proceedings of the IEEE/CVF Conference on Computer Vision and Pattern Recognition*, pp. 4460–4470, June 2019.
- Jeong Joon Park, Peter Florence, Julian Straub, Richard Newcombe, and Steven Lovegrove. DeepSDF: Learning continuous signed distance functions for shape representation. In *Proceedings of the IEEE/CVF Conference on Computer Vision and Pattern Recognition*, pp. 165–174, June 2019.
- Songyou Peng, Michael Niemeyer, Lars Mescheder, Marc Pollefeys, and Andreas Geiger. Convolutional occupancy networks. In *European Conference on Computer Vision*, pp. 523–540. Springer, 2020.
- Songyou Peng, Chiyu Jiang, Yiyi Liao, Michael Niemeyer, Marc Pollefeys, and Andreas Geiger. Shape as points: A differentiable poisson solver. *Advances in Neural Information Processing Systems*, 34:13032–13044, 2021.

- Siyu Ren, Junhui Hou, Xiaodong Chen, Ying He, and Wenping Wang. Geoudf: Surface reconstruction from 3d point clouds via geometry-guided distance representation. In *Proceedings of the IEEE/CVF International Conference on Computer Vision*, pp. 14214–14224, 2023.
- Tianchang Shen, Jun Gao, Kangxue Yin, Ming-Yu Liu, and Sanja Fidler. Deep marching tetrahedra: a hybrid representation for high-resolution 3d shape synthesis. *Advances in Neural Information Processing Systems*, 34:6087–6101, 2021.
- Pei Sun, Henrik Kretschmar, Xerxes Dotiwalla, Aurelien Chouard, Vijaysai Patnaik, Paul Tsui, James Guo, Yin Zhou, Yuning Chai, Benjamin Caine, et al. Scalability in perception for autonomous driving: Waymo open dataset. In *Proceedings of the IEEE/CVF conference on computer vision and pattern recognition*, pp. 2446–2454, 2020.
- Towaki Takikawa, Joey Litalien, Kangxue Yin, Karsten Kreis, Charles Loop, Derek Nowrouzezahrai, Alec Jacobson, Morgan McGuire, and Sanja Fidler. Neural geometric level of detail: Real-time rendering with implicit 3d shapes. In *Proceedings of the IEEE/CVF Conference on Computer Vision and Pattern Recognition*, pp. 11358–11367, 2021.
- Peng Wang, Lingjie Liu, Yuan Liu, Christian Theobalt, Taku Komura, and Wenping Wang. Neus: Learning neural implicit surfaces by volume rendering for multi-view reconstruction. *Advances in Neural Information Processing Systems*, 34:27171–27183, 2021.
- Peng-Shuai Wang, Yang Liu, and Xin Tong. Dual octree graph networks for learning adaptive volumetric shape representations. *ACM Transactions on Graphics*, 41(4):1–15, 2022.
- Yiming Wang, Qin Han, Marc Habermann, Kostas Daniilidis, Christian Theobalt, and Lingjie Liu. Neus2: Fast learning of neural implicit surfaces for multi-view reconstruction. In *Proceedings of the IEEE/CVF International Conference on Computer Vision*, pp. 3295–3306, 2023.
- Jianglong Ye, Yuntao Chen, Naiyan Wang, and Xiaolong Wang. Gifs: Neural implicit function for general shape representation. In *Proceedings of the IEEE/CVF Conference on Computer Vision and Pattern Recognition*, pp. 12829–12839, June 2022.
- Congyi Zhang, Guying Lin, Lei Yang, Xin Li, Taku Komura, Scott Schaefer, John Keyser, and Wenping Wang. Surface extraction from neural unsigned distance fields. In *Proceedings of the IEEE/CVF International Conference on Computer Vision*, pp. 22531–22540, 2023.
- Junsheng Zhou, Baorui Ma, Yu-Shen Liu, Yi Fang, and Zhizhong Han. Learning consistency-aware unsigned distance functions progressively from raw point clouds. *arXiv preprint arXiv:2210.02757*, pp. 1–xxx, 2022.
- Qingnan Zhou and Alec Jacobson. Thingi10k: A dataset of 10,000 3d-printing models. *arXiv preprint arXiv:1605.04797*, 2016.
- Heming Zhu, Yu Cao, Hang Jin, Weikai Chen, Dong Du, Zhangye Wang, Shuguang Cui, and Xiaoguang Han. Deep fashion3d: A dataset and benchmark for 3d garment reconstruction from single images. In *Computer Vision–ECCV 2020: 16th European Conference, Glasgow, UK, August 23–28, 2020, Proceedings, Part I 16*, pp. 512–530. Springer, 2020.

Appendix

A DIFFERENCE FROM GIFS AND UODF

GIFS employs a classifier to predict whether a line segment intersects the surface. If an intersection occurs, the intersection point on the line segment is interpolated using the UDF values of its two endpoints. Then, it modifies the Marching Cubes (MC) algorithm to extract surfaces based on the intersection status of each cube’s edges. In contrast, our SALS predicts an intersection ratio for a given line segment, avoiding the interpolation errors introduced by UDFs, as discussed in Sec. 1. Furthermore, we propose E-DC to extract surfaces directly from our LSF. Experimental results demonstrate the significant advantage of our method in terms of both reconstruction accuracy and efficacy.

For a query point, UODF only predicts its distance to the surface along three fixed directions, making it non-differentiable. Additionally, UODF does not offer a surface extraction method but instead generates a dense point cloud, from which a masked Poisson method is used to reconstruct the mesh. In contrast, our approach samples line segments across the entire space, develops their differentiable properties, and utilizes the custom-designed E-DC for surface extraction.

B SOLUTION OF QEF

QEF can be solved using least squares method,

$$\hat{\mathbf{x}} = (\mathbf{A}^\top \mathbf{A})^{-1} \mathbf{A}^\top \mathbf{B}, \quad (8)$$

where matrix \mathbf{A} and \mathbf{B} are defined as

$$\begin{aligned} \mathbf{A} &= \begin{pmatrix} \dots\dots \\ -o_i \mathbf{n}_i - \\ \dots\dots \end{pmatrix}, \\ \mathbf{B} &= \begin{pmatrix} \dots\dots \\ -o_i \mathbf{p}^\top \mathbf{n}_i - \\ \dots\dots \end{pmatrix}. \end{aligned} \quad (9)$$

Considering that $\mathbf{A}^\top \mathbf{A}$ may be singular, directly calculating its inverse may get wrong results. We first perform eigenvalue decomposition on the matrix,

$$\mathbf{A}^\top \mathbf{A} = \mathbf{U}^\top \mathbf{\Sigma} \mathbf{U}, \quad (10)$$

where \mathbf{U} is an orthogonal matrix and $\mathbf{\Sigma}$ is a diagonal matrix, $\mathbf{\Sigma} = \text{Diag}(\sigma_1, \sigma_2, \sigma_3)$, with $\sigma_1 \geq \sigma_2 \geq \sigma_3$ representing the eigenvalues. Here we define the inverse matrix of $\mathbf{\Sigma}$

$$\mathbf{\Sigma}^{-1} = \begin{pmatrix} \text{Inv}(\sigma_1) & 0 & 0 \\ 0 & \text{Inv}(\sigma_2) & 0 \\ 0 & 0 & \text{Inv}(\sigma_3) \end{pmatrix}, \quad (11)$$

where Inv is defined as

$$\text{Inv}(\sigma) = \begin{cases} 1/\sigma, & \text{if } \sigma > \epsilon \\ 0, & \text{else} \end{cases}. \quad (12)$$

In our experiment, we set $\epsilon = 0.1$.

C NEURAL IMPLICIT REPRESENTATION

Network Details. The last layer of the network uses a sigmoid function to constrain the output to the range $[0,1]$. For the intersection flag, we apply a threshold to binarize the output. If the threshold is set too low, some intersecting line segments may be incorrectly classified as non-intersecting, resulting in holes when extracting the surface using E-DC. The number of holes can be reduced by lowering the threshold for the intersection flag. In our experiments, the threshold was set to 0.1. We have included visual results of the extracted surfaces under different thresholds in Fig. 12.

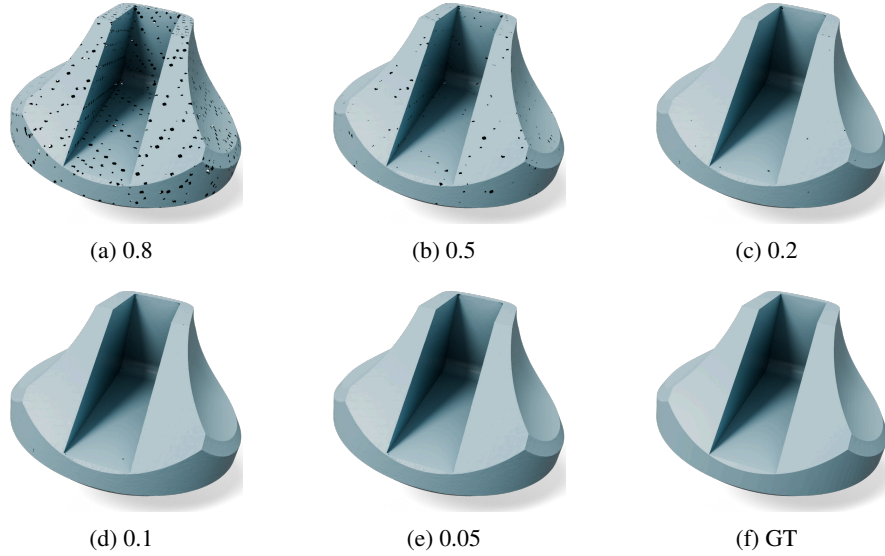


Figure 12: Extracted surfaces under different thresholds for intersection flag.

Error Map. Fig. 13 presents the error maps of the reconstructed models shown in Fig. 6. The results demonstrate that the reconstruction errors of models produced by our method are significantly smaller than those of the baseline methods, particularly in regions with sharp features.

Correctness of Theorem 1. To verify the correctness of Theorem 1, we utilize two different kinds of normal vectors in E-DC, random and zeros, and the visual comparison and error maps are shown in Fig. 14. It can be seen that using the gradient of s as the direction of normal vectors could achieve significant better reconstruction accuracy, demonstrating the correctness of Theorem 1.

Evaluation on Sharp Edges. Following previous methods (Chen et al., 2022), we utilize Edge Chamfer Distance (ECD) and Edge F-score (EF1) to evaluate the preservation of sharp edges. The results on the ABC dataset are shown in Table 6. Clearly, under the evaluation metrics ECD and EF1, our SALS significantly outperforms the baseline methods.

Table 6: Numerical comparison of different methods under ECD and EF1 metrics.

Method	ECD (10^{-2}) \downarrow	EF1 \uparrow
Neural BOF + MC	5.231	0.182
Neural SDF + MC	7.238	0.167
Neural SDF + NDC	2.501	0.526
NGLOD	28.249	0.044
Neural UDF + MeshUDF	6.651	0.169
Neural UDF + NDC	2.632	0.476
Neural UDF + DCUDF	2.828	0.058
Neural UDF + DualMesh	2.870	0.609
UODF	55.823	0.034
SALS (Ours)	1.970	0.601

Different E-DC Resolutions. Fig. 15 demonstrates the visual results of different E-DC resolutions on the selected shapes from the Famous dataset. When the resolution is set to 64, the extracted surfaces do not show significant distortion.

Positional Encoding. Positional Encoding (PE) is a widely adopted technique in implicit representations. However, incorporating PE into our SALS framework leads to a reduction in surface reconstruction quality. As illustrated in Fig. 16, the use of PE introduces floating artifacts around the extracted surface, diminishing the overall representation accuracy.

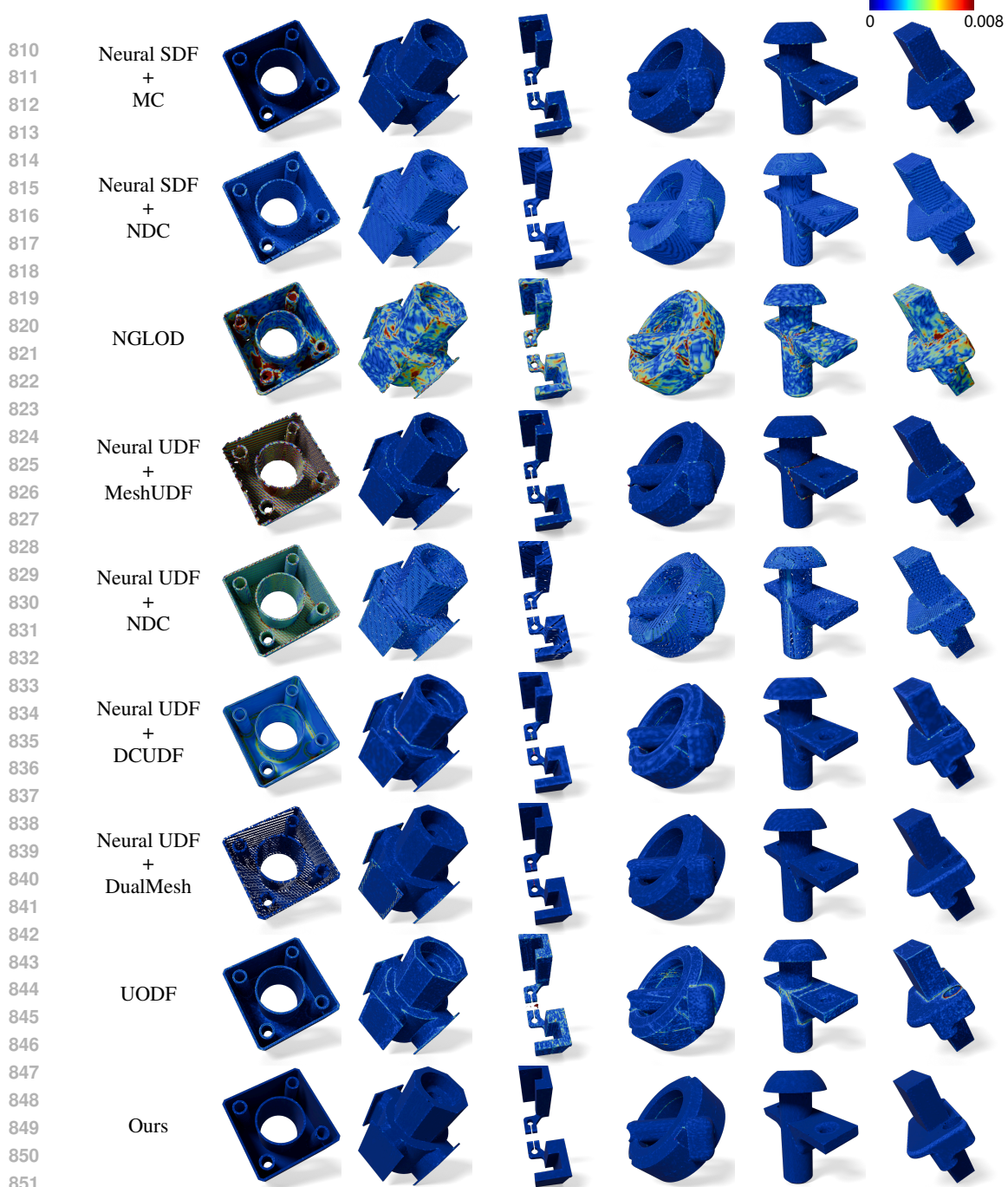


Figure 13: Visual comparisons of different neural implicit representations. [Q](#) Zoom in to see details.

Efficiency Analysis. In the task of neural implicit representation (Sec. 3.3), the time cost consists of two parts, training/overfitting time and surface extraction time. We have recorded the runtime for these two parts, as shown in Table 7. It is worth noting that the resolution of Marching Cubes, Dual Contouring, and our E-DC is 128. During training, our method takes slightly longer compared to neural BOF/SDF/UDF because it processes a 6D input vector and outputs a 2D vector, unlike the latter approaches which take a 3D input vector and produce a scalar output. NGLOD and UODF employ complex architectures, resulting in longer training times. In terms of surface extraction time, our method is slower than MC, MeshUDF, and DualMesh but significantly faster than DCUDF and NDC.

Runtime of E-DC. We measured the runtime for calculating intersection points in each cube and performing triangle extraction, as shown in Table 8. The results demonstrate that our E-DC is

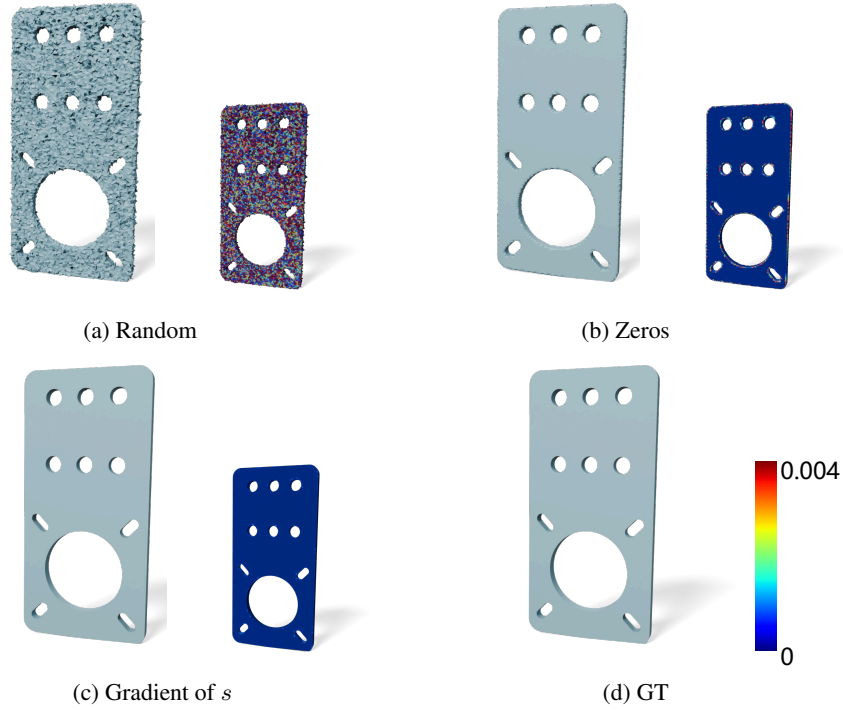


Figure 14: Extracted surfaces using E-DC with different estimated normal vectors. [Q](#) Zoom in to see details.

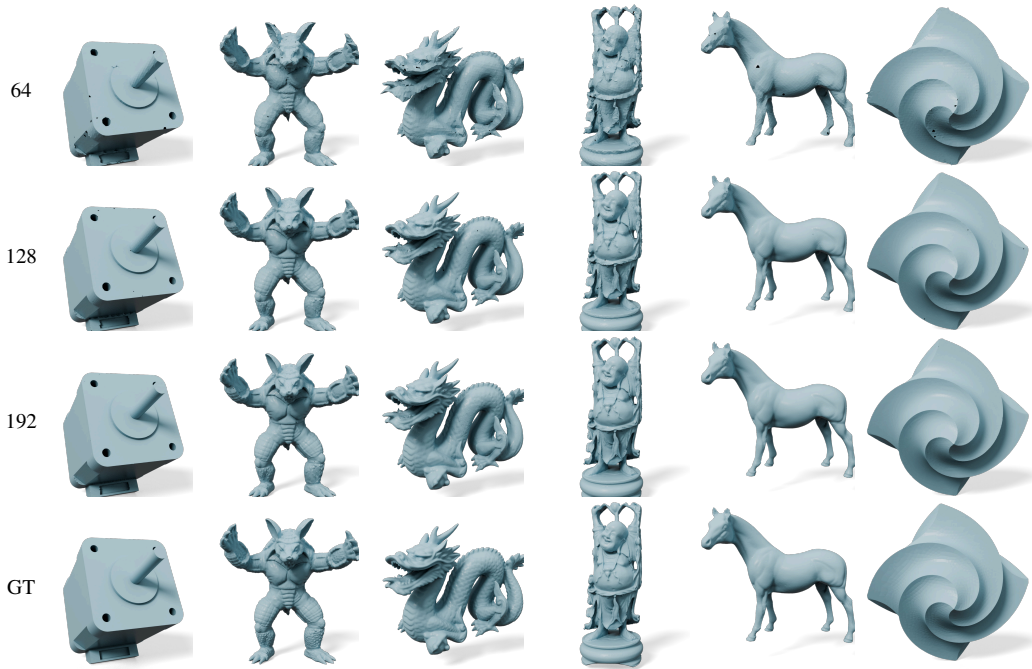


Figure 15: Visual results of different E-DC resolutions on the selected shapes from the Famous dataset.

[Q](#) Zoom in to see details.

faster than NDC in terms of intersection point calculating in each cube and triangle extraction. This efficiency is due to our method not relying on a neural network to estimate the intersection points within each cube.

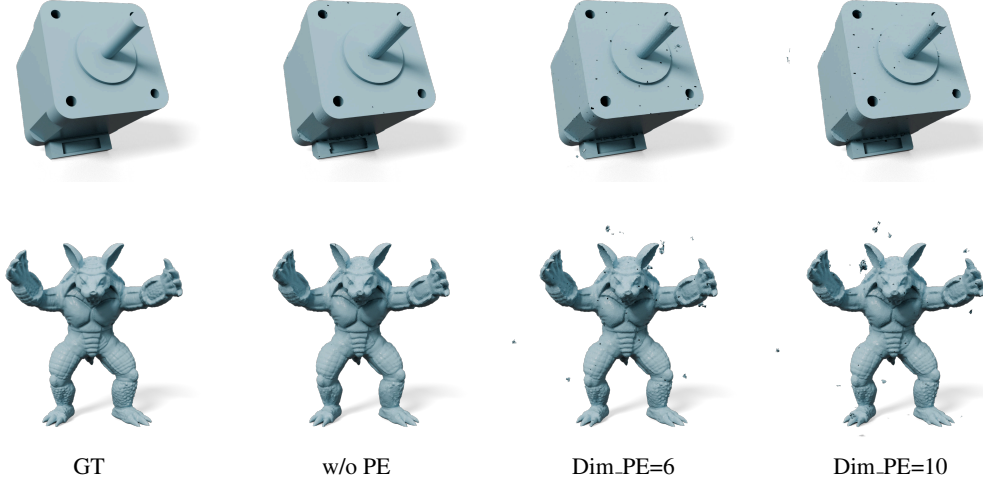


Figure 16: Visual comparison of shape representation with and without PE in the MLP. [Zoom in to see details.](#)

Table 7: Running time of different representation methods.

Method	Training Time (min)	Inference Time (s)
Neural BOF + MC	10.02	0.57
Neural SDF + MC	10.34	0.60
Neural SDF + NDC		7.41
NGLOD	30.14	1.02
Neural UDF + MeshUDF		1.57
Neural UDF + NDC	10.56	6.983
Neural UDF + DCUDF		68.81
Neural UDF + Dual Mesh		1.69
UODF	185.68	10.64
SALS (Ours)	11.56	2.96

D SURFACE RECONSTRUCTION FROM POINT CLOUDS

Error Maps. Fig. 17 shows the error maps of the reconstructed models shown in Fig. 8, demonstrating that the reconstruction errors of the models produced by our method are significantly smaller than those of the baseline methods, especially in regions with sharp features.

Additional Visual Results. Fig. 18 shows additional visual results on the ABC dataset.

Evaluation on Sharp Edges. We utilize ECD and EF1 to evaluate the preservation of sharp edges in the reconstructed surfaces from point clouds. The results on the ABC dataset are shown in Table 9. Clearly, under the evaluation metrics ECD and EF1, our SALS significantly outperforms the baseline methods.

Different Point Cloud Densities. Fig. 19 illustrates the reconstructed surfaces under varying input point cloud densities. Notably, reducing the point cloud density does not lead to a significant drop in reconstruction accuracy, underscoring the robustness of our method to variations in input point cloud density.

Different K -NN Patch Sizes. Fig. 20 shows the reconstructed surfaces under different K -NN patch sizes. We also tested different K -NN patch sizes on point clouds with different densities, the numerical results are shown in Table 10. It can be seen that the variation trend of K -NN patch size is similar across point clouds with different densities and datasets, i.e., too large or small K -NN patch size can lead to a decrease in reconstruction accuracy.

Table 8: Comparison of runtime between NDC and our E-DC..

Method	Calculate Intersection Points (s)	Triangle Extraction (s)	Total Time (s)
NDC	0.151	0.045	0.196
E-DC (Ours)	0.129	0.005	0.134

Figure 17: Visual comparisons of different point cloud surface reconstruction methods. [Zoom in to see details.](#)

Efficiency Analysis. In the task of surface reconstruction from point clouds (Sec. 3.4), the inference times of different methods are shown in Table 11. Our method is comparable to POCO and GeoUDF but faster than GIFS. CAP-UDF is an optimization-based method, which requires more time.

E LIMITATION

Unlike previous implicit representations that primarily focus on individual points in 3D space, our proposed SALS targets line segments in 3D space, which introduces greater complexity. Consequently, when the number of sampled line segments is limited, the network struggles to accurately model the LSF, leading to distortions in the reconstructed surfaces, as shown in Table 12.

Table 9: Numerical comparison of different point cloud surface reconstruction methods under ECD and EF1 metrics.

Method	ECD (1e-2)	EF1
POCO	14.661	0.069
GIFS	7.669	0.105
CAP-UDF	11.022	0.140
GeoUDF	14.818	0.067
Ours	3.480	0.432

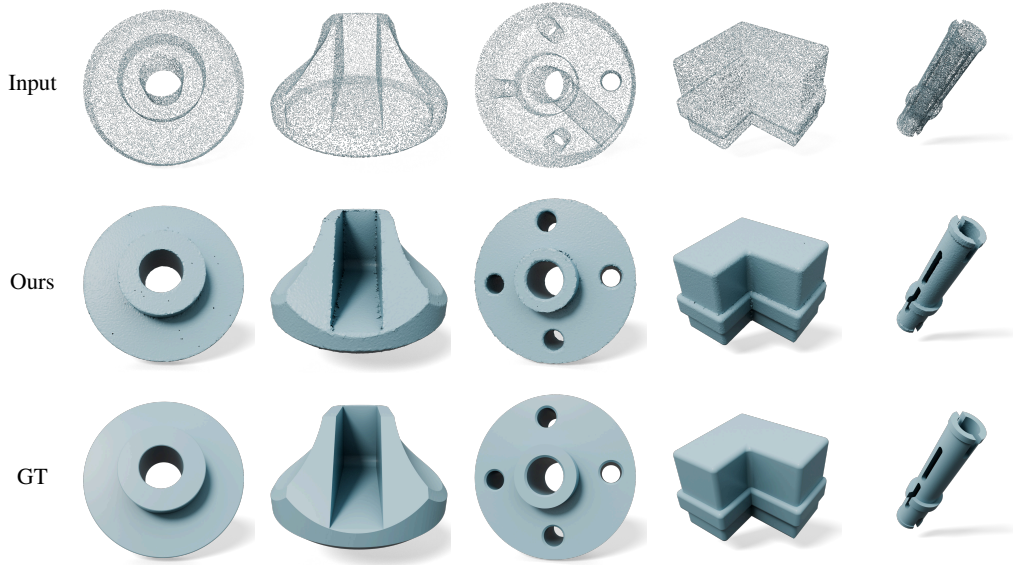


Figure 18: Additional visual results on the ABC dataset. [Q Zoom in to see details.](#)

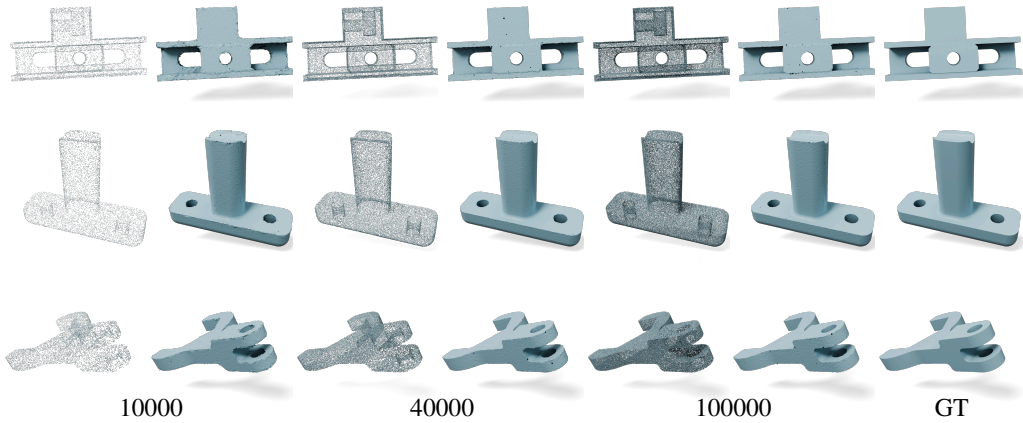


Figure 19: Visual results of different input point cloud densities. [Q Zoom in to see details.](#)

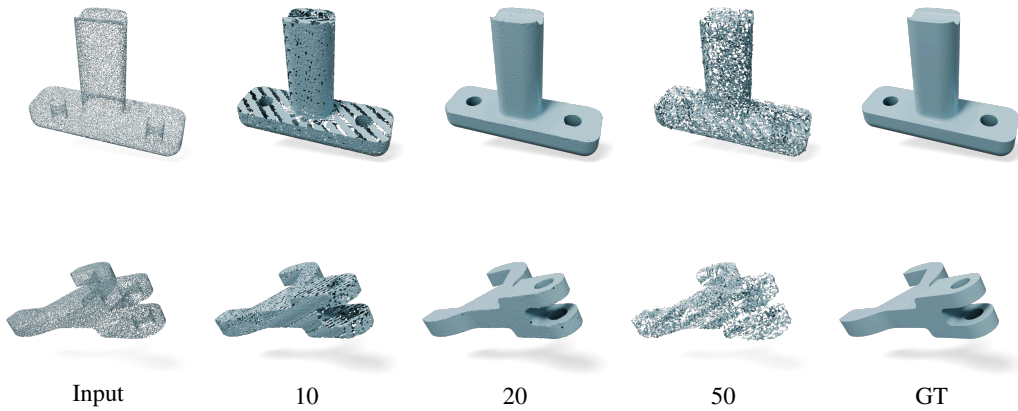


Figure 20: Visual comparison of reconstructed surfaces under different K -NN patch sizes. [Q Zoom in to see details.](#)

Table 10: Surface reconstruction of point clouds with varying densities under different K -NN sizes.

Dataset	# Points	K	CD (10^{-3}) \downarrow	NC	F1-0.005 \uparrow	F1-0.01 \uparrow
ABC	10000	10	9.852	0.840	0.367	0.685
		20	4.842	0.953	0.608	0.948
		50	11.504	0.609	0.163	0.524
	40000	10	6.367	0.903	0.489	0.848
		20	4.560	0.973	0.630	0.962
		50	14.370	0.657	0.164	0.415
	100000	10	5.547	0.930	0.541	0.902
		20	4.514	0.977	0.636	0.964
		50	29.224	0.643	0.068	0.170
non-manifold ABC	10000	10	13.956	0.754	0.188	0.512
		20	6.992	0.857	0.441	0.818
		50	13.466	0.576	0.088	0.399
	40000	10	8.502	0.845	0.291	0.724
		20	6.033	0.951	0.425	0.883
		50	14.565	0.650	0.144	0.456
	100000	10	8.494	0.845	0.291	0.725
		20	4.733	0.956	0.613	0.949
		50	14.562	0.651	0.144	0.456

Table 11: Running time of different point cloud surface reconstruction methods.

Method	POCO	GIFS	CAP-UDF	GeoUDF	SALS (Ours)
Inference Time (s)	13.66	45.57	906.34	15.269	14.38

Table 12: Numerical results under different numbers of samples.

# Samples	CD (10^{-3}) \downarrow	NC	F1-0.005 \uparrow	F1-0.01 \uparrow
100K	19.200	0.778	0.304	— 0.565
500K	8.086	0.923	0.542	0.862
1M	5.242	0.962	0.609	0.937
5M	4.623	0.976	0.630	0.959
10M	4.493	0.980	0.638	0.965
20M	4.691	0.975	0.629	0.956
40M	4.534	0.979	0.635	0.963